

RESEARCH ARTICLE

10.1002/2015JB012419

Key Points:

- Temporal variation of tropospheric delay includes systematic and stochastic components
- Time series of wet delay from satellite spectrometers can quantify the InSAR uncertainty
- The uncertainty of the InSAR displacement and velocity is dominated by the stochastic delay

Supporting Information:

- Figures S1–S4

Correspondence to:

H. Fattahi,
hfattahi@gps.caltech.edu

Citation:

Fattahi, H., and F. Amelung (2015), InSAR bias and uncertainty due to the systematic and stochastic tropospheric delay, *J. Geophys. Res. Solid Earth*, 120, doi:10.1002/2015JB012419.

Received 3 AUG 2015

Accepted 23 NOV 2015

Accepted article online 27 NOV 2015

InSAR bias and uncertainty due to the systematic and stochastic tropospheric delay

Heresh Fattahi^{1,2} and Falk Amelung¹

¹Rosenstiel School of Marine and Atmospheric Science, University of Miami, Miami, Florida, USA, ²Now at Seismological Laboratory, California Institute of Technology, Pasadena, California, USA

Abstract We quantify the bias and uncertainty of interferometric synthetic aperture radar (InSAR) displacement time series and their derivatives, the displacement velocities, by analyzing the systematic and stochastic components of the temporal variation of the tropospheric delay. The biases due to the systematic seasonal delay depend on the SAR acquisition times, whereas the uncertainties depend on the standard deviation of the random delay, the number of acquisitions, the total time span covered, and the covariance of the time series of the stochastic delay between a pixel and the reference. We study the contribution of the wet delay to the InSAR observations along the western India plate boundary using (i) Moderate Resolution Imaging Spectroradiometer precipitable water vapor, (ii) stratified tropospheric delay estimated from the ERA-I global atmospheric model, and (iii) seven Envisat InSAR swaths. Our analysis indicates that the amplitudes of the annual delay vary by up to ~10 cm in this region equivalent to a maximum displacement bias of ~24 cm in InSAR line of sight direction between two epochs (assuming Envisat IS6 beam mode). The stratified tropospheric delay correction mitigates this bias and reduces the scatter due to the stochastic delay. For ~7 years of Envisat acquisitions along the western India plate boundary, the uncertainty of the InSAR velocity field due to the residual stochastic wet delay after stratified tropospheric delay correction using the ERA-I model is in the order of ~2 mm/yr over 100 km and ~4 mm/yr over 400 km. We discuss the implication of the derived uncertainties on the full variance-covariance matrix of the InSAR data.

1. Introduction

Interferometric synthetic aperture radar (InSAR) potentially delivers accurate (millimeter level) fields of ground displacement over large areas (hundreds of kilometers) [Massonnet and Feigl, 1998; Rosen et al., 2000; Hanssen, 2001] and has been widely used to study earthquakes [Simons et al., 2002; Funning et al., 2005; Calais et al., 2010], volcanoes [Chaussard et al., 2013; Pritchard et al., 2013], tectonic deformation [Biggs et al., 2007; Wang et al., 2009], and land subsidence [Amelung et al., 1999; Dehghani et al., 2009]. The accuracy of the InSAR measurements is affected by phase decorrelation [Zebker and Villasenor, 1992], orbital errors, topographic residuals, phase-unwrapping errors, imperfect simulation of the imaging geometry, and extra path delay due to the propagation of the microwave signal through the atmosphere [Goldstein, 1995; Massonnet and Feigl, 1995; Tarayre and Massonnet, 1996; Zebker et al., 1997; Hanssen, 2001].

Significant progress has been made in the past decade and a half to improve the measurement accuracy. Topographic residuals can be corrected for by simultaneous analysis of a time series of SAR acquisitions [Ferretti et al., 2001; Berardino et al., 2002; Samsonov, 2010; Fattahi and Amelung, 2013]. It has been shown that for modern satellites with precise orbits, the effect of orbital errors is small. Typical velocity uncertainties are less than 0.5 mm/yr over 100 km distance [Fattahi and Amelung, 2014]. For the Envisat SAR sensor, biases affecting the simulation of the imaging geometry including a drift of the local oscillator and timing error were identified [Marinkovic and Larsen, 2013; Fattahi and Amelung, 2014; Wang and Jonsson, 2014]. Atmospheric delays remain the main source of uncertainty for InSAR measurements.

Propagation of the microwave signal through the atmosphere is affected by the free electrons in the ionosphere and by the electrically neutral atmosphere, which mainly includes the troposphere. The ionosphere is a dispersive medium, which means that the free electrons of the ionosphere cause a frequency-dependent phase advance or a group delay [Mendes, 1999]. Several methods are available to correct the ionospheric contribution [e.g., Mattar and Gray, 2002; Rosen et al., 2010; Chen et al., 2012, 2014; Liu et al., 2014]. In contrast, the troposphere causes a nondispersive delay due to the higher refractivity compared to vacuum.

Several strategies have been pursued to mitigate the tropospheric delays in the InSAR data. The first relies on abundant SAR acquisitions averaging out the tropospheric delays of individual acquisitions using simple stacking of multiple interferograms [Schmidt *et al.*, 2005; Wei *et al.*, 2010], or spatial-temporal filtering of the time series [Ferretti *et al.*, 2001; Bernardino *et al.*, 2002], ignoring the fact that tropospheric delay is not Gaussian distributed. Advanced filtering approaches use statistical representation of the delay to optimize the filtering parameters [Liu, 2012; Gong *et al.*, 2015]. The second strategy is based on the interpolation of the estimated tropospheric delay from GPS observations to form delay maps and correct InSAR observations [Onn and Zebker, 2006; Löfgren *et al.*, 2010]. The third strategy uses observations of atmospheric water vapor from satellite spectrometers such as the Medium-Resolution Imaging Spectrometer (MERIS) data from the Envisat satellite [Li *et al.*, 2005, 2006; Walters *et al.*, 2013] and the Moderate Resolution Imaging Spectroradiometer (MODIS) observations from the Aqua and Terra satellites [Li *et al.*, 2005, 2009]. Tropospheric delay correction with the multispectral imagery is limited to daylight hours and cloud-free conditions.

A fourth approach divides the tropospheric delay into stratified and nonstratified components and estimates the stratified delay from the InSAR data [e.g., Doin *et al.*, 2009]. Although this approach significantly reduces the stratified tropospheric delay in regions with extreme topography variations [Grandin *et al.*, 2012], it cannot distinguish the stratified delay from ground displacement correlated with topography [Doin *et al.*, 2009; Fournier *et al.*, 2011]. The performance of the empirical approach has been improved by using a multiscale approach with band-pass decomposition of both topography and InSAR phase observations [Lin *et al.*, 2010] and by using a spatially variable power law approach [Bekaert *et al.*, 2015a].

Since the tropospheric delay is a deterministic component of the InSAR phase observations, its contribution can in principle be mitigated using information about the atmospheric fields. A fifth strategy uses numerical weather models. Two types of models have been used: (i) global atmospheric reanalysis models with low spatial and temporal resolution such as the ERA-I model of the European Centre for Medium-Range Weather Forecasts [Dee *et al.*, 2011] and (ii) high spatial and temporal resolution weather forecast models obtained by nesting grids within coarser models [Webley *et al.*, 2004; Foster *et al.*, 2006, 2013; Puyssegur *et al.*, 2007; Wadge *et al.*, 2010; Eff-Darwich *et al.*, 2012].

In practice, however, numerical weather models have produced mixed results. Jolivet *et al.* [2011, 2014] report on successful correction of long-wavelength stratified tropospheric delay in different regions using global atmospheric models including ERA-I and Modern-Era Retrospective Analysis for Research And Applications. Cong *et al.* [2012] uses weather models for precise geolocation. Hobiger *et al.* [2010] emphasizes the need of accurate ray tracing when high spatial resolution models are used. Walters *et al.* [2013] conclude that for their test area the tropospheric delay correction using the ERA-I model is unsatisfactory, compared to using MERIS observations. Foster *et al.* [2013] do not find any benefits from using numerical weather models in the Mount St. Helens region. Liu [2012] reports successful use of numerical weather models in mountainous regions but not for flat areas. Several other studies reported varying degrees of success [Li *et al.*, 2009; Kinoshita *et al.*, 2013; Samsonov *et al.*, 2014]. A common limitation of previous studies is that the uncertainties of the corrections and of the corrected InSAR displacements and/or velocities were not considered.

The uncertainty due to the tropospheric delay of InSAR measurements of ground deformation depends on the spatial and temporal variation of the tropospheric delay. To evaluate the uncertainty, we subdivide the delay into systematic and stochastic components in both space and time. Several studies have investigated these components in space [e.g., Hanssen, 2001; Emardson, 2003; Liu, 2012]. Here we investigate them as a function of time, building on the work of Doin *et al.* [2009] and Samsonov *et al.* [2014]. We develop an approach to obtain uncertainties for InSAR displacement time series and velocities using independent delay observations from MODIS and using global atmospheric models. Moreover, we quantify the uncertainties of InSAR time series corrected for stratified tropospheric delay.

2. Tropospheric Delay Affecting InSAR Observations

The double-difference InSAR phase observations between two pixels and two epochs measure the relative change in the distance or range from the radar antenna to the target, hereafter referred to as range change. After correction for the imaging geometry, the range change contains information about ground displacement and about the atmospheric delay in the ionosphere and troposphere. The ionospheric contributions are not considered further in this paper as their impact on the C band SAR data is small. The contribution from

tropospheric delay to the range change observations between two given pixels p and q and between SAR acquisition times t_i and t_j is the integral of the spatial and temporal differences of refractivity over the range from the radar to the pixels, ρ , as [e.g., *Hanssen, 2001*]

$$\delta L_{pq}^{t_i, t_j} = \left[\int_0^{\rho_p} N(\rho, t_j) d\rho - \int_0^{\rho_p} N(\rho, t_i) d\rho \right] - \left[\int_0^{\rho_q} N(\rho, t_j) d\rho - \int_0^{\rho_q} N(\rho, t_i) d\rho \right] \quad (1)$$

where ρ_p and ρ_q are the range from the radar to the pixels p and q , respectively, and $N(\rho, t)$ is the refractivity at time t and range ρ from the radar. Ignoring the water content of clouds and neglecting the compressibility of air and water vapor, refractivity in neutral atmosphere (troposphere) is given by

$$N = K_1 \frac{P_d}{T} + K_2 \frac{e}{T} + K_3 \frac{e}{T^2} \quad (2)$$

where P_d is the partial pressure of dry air; T is the temperature; e is the partial pressure of water vapor; and K_1 , K_2 , and K_3 are empirical constants [*Smith and Weintraub, 1953*]. The first term on the right-hand side of equation (2) gives the refractivity due to the dry air, and the other two terms give the refractivity due to the moist air. Substituting the refractivity due to dry and wet air in equation (1) gives the hydrostatic and wet delay, respectively. Although the absolute hydrostatic delay (a few meters) is much larger than the absolute wet delay (usually less than 0.3 m), its temporal and spatial variation is significantly smaller than for the wet delay. Therefore, the effect of the hydrostatic delay on InSAR is small compared to the wet delay. In this paper we mostly consider wet delay.

In the following we evaluate the temporal variation of the wet delay using time series of zenith wet delay (ZWD) obtained from MODIS observations and from the ERA-I atmospheric model. We use the approach of *Jolivet et al. [2014]* to calculate the ZWD from the ERA-I model, in which e , T , and P_d are interpolated horizontally in space and vertically from ground to a reference elevation above which the variation of the troposphere is assumed to be negligible. Given vertical profiles of e , T , and P_d and given empirical gas constants, the tropospheric delay (one way) is estimated by substituting equation (2) in equation (1) with integration of refractivity in vertical direction and then mapping to the line of sight (LOS) direction. For the time series of ZWD from MODIS, we convert the MODIS precipitable water vapor products to ZWD (one way in centimeters) as $ZWD = \Pi \times PWV$, where Π is the conversion factor assuming a fixed value of $\Pi = 6.2$ [*Bevis et al., 1994; Li et al., 2006*].

3. Uncertainty and Bias

The tropospheric wet delay can be divided into systematic and stochastic components in both space and time. In space, the delay includes stratified (systematic) and turbulent (stochastic) components and in time contains the seasonal (systematic) and nonseasonal (stochastic) components. In the following we consider the systematic and stochastic components in time. We develop an approach to evaluate the bias due to the systematic component and the uncertainty due to the stochastic component. We first assume that the systematic component is periodic and dominated by seasonal variations (section 3.1). We then consider tropospheric delay correction using global atmospheric models and investigate the uncertainties due to the residual delay after the correction (section 3.2). Finally, we estimate the uncertainties directly from the scatter of the InSAR range change time series (section 3.3) and compare with the uncertainties based on the tropospheric information.

3.1. Uncertainty and Bias Without Tropospheric Delay Correction

3.1.1. Bias Due To Seasonal Tropospheric Wet Delay

To demonstrate the effect of seasonal tropospheric wet delay, we model the seasonal component of the time series of ZWD for a given pixel by a summation of sine and cosine functions with annual and semiannual periodicities as

$$ZWD^S(t) = b + \sum_{k=1}^2 S_k \sin(2\pi kt) + C_k \cos(2\pi kt) \quad (3)$$

with b the intercept; S_1 , C_1 the coefficients of the annual components; and S_2 , C_2 the coefficients of the semiannual components, from which their amplitudes (A_1 and A_2) and phases (ϕ_1 and ϕ_2) can be calculated as

$$A_k = \sqrt{S_k^2 + C_k^2}, \phi_k = \tan^{-1} \left(\frac{S_k}{C_k} \right), k = 1, 2 \quad (4)$$

The bias on displacement at a given pixel relative to a reference pixel and between two epochs depends on the differences in amplitude between the two pixels and varies with acquisition time. The bias of the InSAR velocity between two pixels (pixels p and q) is given for a set of N acquisitions with acquisition times of t_1 to t_N , by linear regression of the difference of $A_k \sin(2\pi kt_i + \phi_k)$ between the two pixels as

$$\gamma_k^{p,q} = \frac{\sum_{i=1}^N t_i A_k^{p,q} \sin(2\pi kt_i + \phi_k^{p,q}) - \bar{t} \sum_{i=1}^N A_k^{p,q} \sin(2\pi kt_i + \phi_k^{p,q})}{\sum_{i=1}^N (t_i - \bar{t})^2} \quad (5)$$

with $k = 1, 2$, where $\gamma_1^{p,q}$ and $\gamma_2^{p,q}$ are the velocity bias between pixels p and q due to the annual and semiannual delays, respectively, and \bar{t} is the average of acquisition times as $\bar{t} = \sum_{i=1}^N t_i / N$. $A_k^{p,q}$ and $\phi_k^{p,q}$ are the difference in the amplitude and phase of the annual ($k = 1$) or semiannual delay ($k = 2$) between the two pixels (pixels p and q). This equation shows that the bias is linear in both the delay amplitude difference and the inverse of the total time span covered by the acquisitions (the deviations of the acquisition times from the mean) and nonlinear in the acquisition times.

3.1.2. Uncertainty Due To the Random Tropospheric Delay

To understand the displacement uncertainty due to the stochastic component of the tropospheric delay, we consider the residual slant wet delay, RSWD, obtained by removing the seasonal components from the ZWD and projecting into the slant direction

$$\text{RSWD}(t) = \left(\text{ZWD}(t) - \sum_{k=1}^2 (S_k \sin(2\pi kt) + C_k \cos(2\pi kt)) \right) / \cos(\vartheta) \quad (6)$$

where ϑ is the average incidence angle. The standard deviation of the time series of RSWD for a given pixel at location p , $\sigma_{\text{RSWD}(p)}$, represents the scatter of the random component of the tropospheric delay. To quantify the effect on relative InSAR measurements, we evaluate the variance of the difference in RSWD between pixels p and q , $\sigma_{\text{RSWD}(p) - \text{RSWD}(q)}$, given as

$$\sigma_{\text{RSWD}(p) - \text{RSWD}(q)}^2 = \sigma_{\text{RSWD}(p)}^2 + \sigma_{\text{RSWD}(q)}^2 - 2\eta_{\text{RSWD}(p), \text{RSWD}(q)} \quad (7)$$

where $\sigma_{\text{RSWD}(p)}^2$ and $\sigma_{\text{RSWD}(q)}^2$ are the variance of the absolute RSWD at pixels p and q , respectively, and $\eta_{\text{RSWD}(p), \text{RSWD}(q)}$ the covariance of the time series of RSWD between the two pixels. Due to the spatial correlation of tropospheric delay, the covariance is nonzero and not negligible. Note that $\sigma_{\text{RSWD}(p)}^2$ and $\sigma_{\text{RSWD}(q)}^2$ are variances of absolute stochastic delay at pixels p and q , respectively, while $\sigma_{\text{RSWD}(p) - \text{RSWD}(q)}^2$ is the variance of relative delay between pixels p and q . The covariance component by definition is a relative quantity between two pixels, and the covariance of the delay between a pixel and itself is equal to the variance of the absolute delay at that pixel ($\eta_{\text{RSWD}(p), \text{RSWD}(p)} = \sigma_{\text{RSWD}(p)}^2$).

We refer to $\sigma_d = \sigma_{\text{RSWD}(p) - \text{RSWD}(\text{ref})}$ as the uncertainty for the displacement between a given pixel and a reference pixel at location ref. σ_d represents the scatter due to the stochastic component of the tropospheric delay between the two pixels. Assuming Gaussian white noise, we obtain the uncertainty for the InSAR velocity between a given pixel and the reference, σ_v , by linear error propagation as

$$\sigma_v = \sigma_d / \sqrt{\sum_{i=1}^N (t_i - \bar{t})^2} \quad (8)$$

This equation shows that σ_v depends on σ_d , and inversely on the number of SAR acquisitions and the total time span covered by the acquisitions. σ_d and σ_v are the uncertainties of the InSAR displacement time series and velocity fields, respectively, due to the stochastic component of the delay before any tropospheric delay correction of the InSAR data. Both uncertainties are relative to the reference pixels.

3.2. Uncertainty After Stratified Tropospheric Delay Correction Using Low-Resolution Atmospheric Models

Global atmospheric models have been successfully used to reduce the tropospheric delay in InSAR data [e.g., Jolivet *et al.*, 2011, 2014; Liu, 2012]. The models are interpolated in horizontal and vertical directions based on

the higher-resolution digital elevation models assuming stratified troposphere [e.g., Jolivet *et al.*, 2011, 2014], and then the interpolated zenith delay is projected in slant direction and subtracted from the InSAR data. This procedure is referred to in this paper as stratified tropospheric delay correction. The quality of the correction depends on the spatial and temporal resolution and on the accuracy of the atmospheric model. The stratified delay correction is expected to account for the topography-correlated and long-wavelength components of the tropospheric delay. After correction, the InSAR range change time series remain affected by the nonstratified, turbulent delays, not included in the stratified delay correction from models, and by the residual stratified delay due to the inaccuracy and the low spatial and temporal resolution of the models.

To understand the uncertainty of the InSAR displacement time series and velocity after stratified tropospheric delay correction, we assume that the wet delay observed with MODIS provides the truth and evaluate how it can be approximated by the stratified delay from the ERA-I model. This assumption is valid because the wet delay obtained from MODIS captures both the stratified and nonstratified components of the delay, while the correction obtained from ERA-I carries only the stratified component [e.g., Jolivet *et al.*, 2014]. Also, the MODIS observations have much higher spatial resolution of ~ 1 km compared to ~ 70 km of ERA-I. Moreover, several studies have confirmed the accuracy of MODIS-measured wet delay using independent observations [e.g., Li *et al.*, 2003; Prasad and Singh, 2009; Thomas *et al.*, 2011; Lu *et al.*, 2011]. They found that MODIS slightly overestimates precipitable water vapor by at most a few millimeters and the reported bias varies in different regions. Due to the lack of field observations in the western India plate boundary, we ignore the bias in MODIS data. The small bias is not expected to significantly affect our analysis of the scatter of the delay over few years.

Given the time series of zenith wet delays obtained from MODIS (ZWD^{MODIS}) and ERA-I ($ZWD^{\text{ERA-I}}$), we consider another approach to obtain the residual slant wet delay as

$$\text{RSWD}(t) = (ZWD^{\text{MODIS}}(t) - ZWD^{\text{ERA-I}}(t)) / \cos(\vartheta) \quad (9)$$

We assume that the $ZWD^{\text{ERA-I}}$ mitigates the systematic component of the delay, implying that any bias is eliminated and that RSWD represents the residual stochastic component. We show in section 4 that this assumption is valid and will discuss the caveats of this assumption in section 5.4. The standard deviation of the time series of RSWD between each pixel and the reference pixel, $\sigma_d = \sigma_{\text{RSWD}(p) - \text{RSWD}(\text{ref})}$, represents the scatter of InSAR displacement time series between a given pixel and a reference pixel at location ref after stratified delay correction.

Given a set of SAR acquisitions and assuming that the residual is white noise, we can obtain σ_v using equation (8). σ_d and σ_v are the uncertainties of the InSAR displacement time series and velocity, respectively, due to the residual tropospheric wet delay after the stratified tropospheric delay correction using the ERA-I global atmospheric model.

3.3. Uncertainty of InSAR Velocity From Range Change Time Series

An InSAR range change time series between two coherent pixels, corrected for imaging geometry and atmospheric delay, contains components from ground displacement and residual noise due to imperfect models for the imaging geometry and atmospheric delay. Here we ignore phase decorrelation and phase-unwrapping errors. The velocity of linear displacement can be estimated as the slope of the best fitting line to the range change time series. The uncertainty of the velocity σ_v^{insar} is given as

$$\sigma_v^{\text{insar}} = \frac{\sqrt{\sum_{i=1}^N (d_i - \hat{d}_i)^2}}{\sqrt{(N-2) \sum_{i=1}^N (t_i - \bar{t})^2}} \quad (10)$$

where d_i is the range change at epoch i and \hat{d}_i the predicted linear range change. The other symbols are defined above. σ_v^{insar} represents the uncertainty due to the temporally random residual noise in InSAR range change time series at a given pixel relative to a reference pixel. σ_v^{insar} does not describe the uncertainty due to the temporally correlated noise.

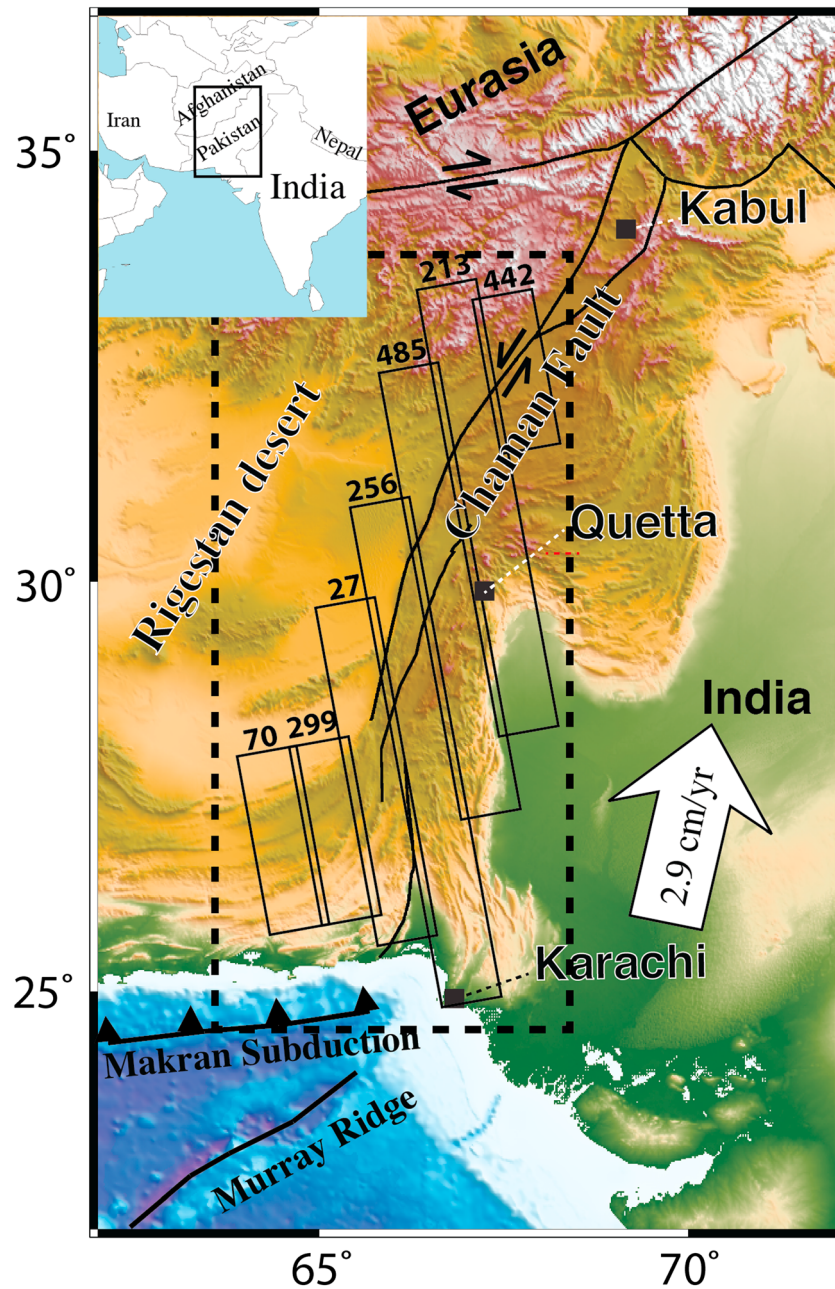


Figure 1. Western India plate boundary in Afghanistan and Pakistan. The black dashed box shows the region of Figures 4, 5, and 6. The solid boxes show the footprint of ascending Envisat tracks across the Chaman Fault system, the boundary between India and Eurasia.

4. Application to the Western India Plate Boundary Zone

We evaluate the atmospheric contribution to the uncertainty of InSAR displacement and velocity measurements using MODIS wet delay observations and delays from numerical weather prediction models. We evaluate the uncertainties both before and after stratified tropospheric delay correction for the western India plate boundary zone (Figure 1). Our wet delay truth consists of daily 2002–2011 precipitable water vapor observations by MODIS (precipitable water vapor (PWV) products). More than 75% of all the pixels have at least 2500 cloud-free acquisitions (see Figure S1 in the supporting information for a map of the number of cloud-free acquisitions). We use the ERA-I model to calculate the daily stratified tropospheric wet delay at 6:00 A.M. UTC (11:00 A.M. local time), which is the model output time closest

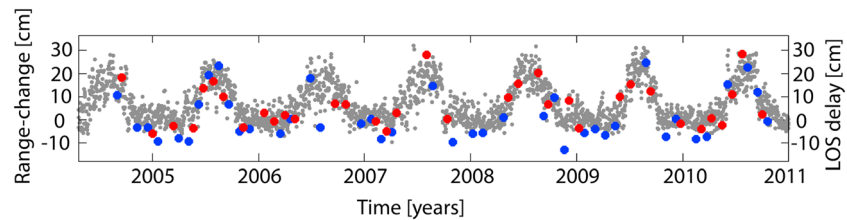


Figure 2. InSAR LOS range change time series between two pixels in the overlapping area of tracks 27 (red circles) and 256 (blue circles) superimposed on the relative time series of stratified tropospheric delay from ERA-I between the two pixels (hydrostatic + wet, grey dots, [latitude, longitude] locations at [25.99, 66.57] and [29.2, 65.91], elevation difference of 1060 m). The InSAR data are corrected for local oscillator drift and topographic residuals. The InSAR time series have been aligned to ERA-I by adding constants representing the delays of the first epochs.

to the MODIS acquisitions (~10:00 A.M. local time). Such time difference can potentially affect the performance of atmospheric corrections, but addressing this would be beyond the scope of this paper. However, the 1 h time difference between MODIS and ERA-I does not affect our evaluations of the seasonal delay and the standard deviation of the temporal stochastic component of the delay over few years.

The InSAR data consist of ~7 years (2004 to 2011) ascending Envisat advanced synthetic aperture radar (ASAR) acquisitions from tracks 70 (frames 495, 513, and 531), 299 (frames 495, 513, and 531), 27 (frames 495, 513, 531, 549, and 567), 256 (frames 477, 495, 513, 531, 549, 567, and 585), 485 (frames 531, 549, 567, 585, 603, and 621), 213 (frames 567, 585, 603, 621, and 639), and 442 (frames 621 and 639) (beam IS6). For each track we generate connected networks of small baseline interferograms (see Figure S2 for the network). We correct the interferograms for possible phase-unwrapping errors using a phase closure approach [Fattahi, 2015] and invert for the range change time series. The connected networks result in full-rank design matrices, ensuring unbiased estimation of range change time series. It is important that the networks are connected, because nonlinear phase contributions from tropospheric delay and topographic residuals at network discontinuities bias the estimated range change time series. We correct the time series for local oscillator drift [Marinkovic and Larsen, 2013], topographic residuals [Fattahi and Amelung, 2013] and remove the wet and hydrostatic stratified tropospheric delay using the ERA-I model [Jolivet et al., 2014]. Incoherent pixels are masked out using a temporal coherence threshold of 0.7 [Pepe et al., 2006]. For processing details see Fattahi [2015].

4.1. Systematic and Stochastic Components of Wet Delay Between Two Pixels

The InSAR range change time series between two pixels, ~360 km away and with an elevation difference of 1060 m, is dominated by seasonal variations of tropospheric delay as shown by the comparison with the sum of wet and hydrostatic delay from ERA-I (Figure 2). The time series of the MODIS-observed wet delay difference in slant direction between the two pixels is characterized by annual and semiannual amplitudes of 7.3 cm and 1.5 cm, respectively (Figure 3a). The corresponding displacement biases between SAR acquisitions from the trough and the peak of a seasonal cycle are 14.6 and 3 cm, respectively. Using equation (5), we find that sampling with acquisition times of track 256 and track 27 lead to velocity biases of 3.5 mm/yr and 1 mm/yr, respectively. Using as an example the acquisition times from both the tracks, the bias is 1.2 mm/yr, which is larger than the bias obtained from the acquisition times of track 27. This example demonstrates that more acquisitions do not always reduce the bias.

To evaluate the stochastic component, we remove the seasonal variation from the slant wet delay using equation (6) (red time series in Figure 3a), transforming the distribution of the delay from skewed (Figure 3b) into Gaussian (Figure 3c, standard deviation of 5.8 cm). From the delay distributions, we infer that the residual can be considered as stochastic. The difference of the wet delay from MODIS and ERA-I (green time series in Figure 3a) is also Gaussian distributed (Figure 3d). Its smaller standard deviation of 4.8 cm indicates that the stratified tropospheric delay correction with ERA-I not only mitigates the periodic delay but also reduces the uncertainty due to the stochastic component. A standard deviation of 4.8 cm implies a displacement uncertainty of 9.6 cm at 68% confidence level and of 14.4 cm at 95% confidence level between any two epochs.

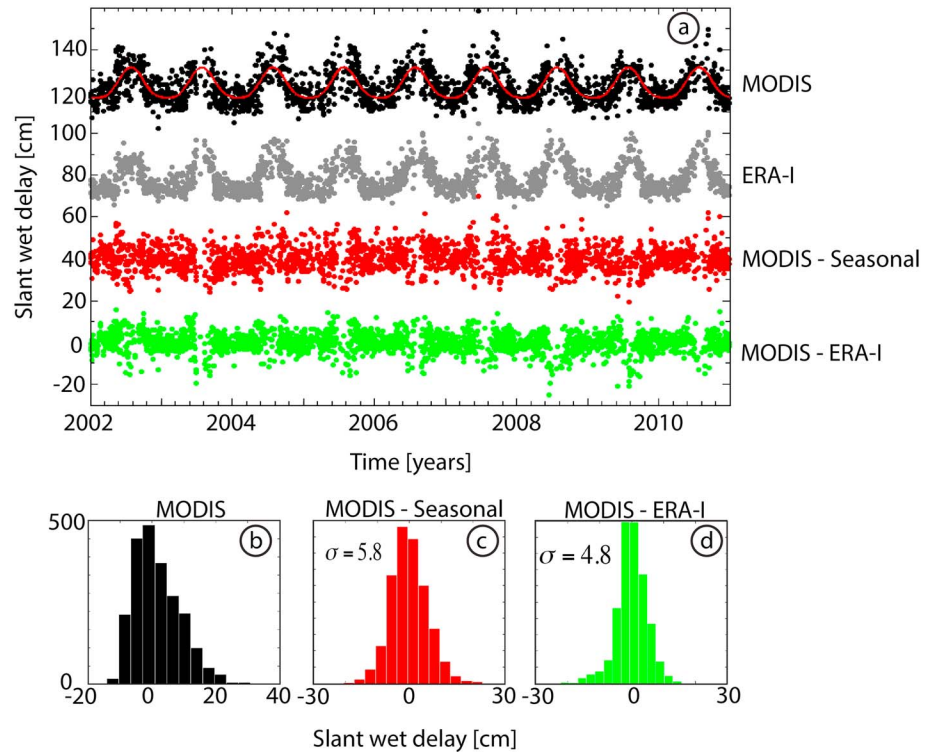


Figure 3. (a) Time series of relative slant wet delay from MODIS (black), ERA-I (grey), the residual of MODIS and best fitted seasonal delay (red), and the residual of MODIS and ERA-I (green). MODIS time series is superimposed by the best fitted seasonal delay (red line) with annual and semiannual amplitudes of 7.3 and 1.5 cm, respectively. The time series of relative delay are between the same two points as Figure 2 and have been shifted in y axis by arbitrary offsets for display. (b) Distribution of relative slant wet delay from MODIS, (c) the residual of MODIS and best fitted seasonal delay, and (d) the residual of MODIS and ERA-I.

4.2. Bias and Uncertainty of InSAR Displacement Across the Whole Area

4.2.1. Without Tropospheric Delay Correction

Our approach to understand the contribution of the tropospheric delay to the InSAR data before tropospheric delay correction is to distinguish between the bias caused by the seasonal component of the delay and the uncertainty due to the stochastic component. We first evaluate the amplitude of the seasonal delay obtained from the time series of MODIS observations and then analyze the uncertainty due to the stochastic component from RSWD, which is obtained after removing the seasonal delay from the ZWD.

Figures 4a and 4b show maps of the amplitude of the annual and semiannual absolute zenith wet delay obtained from MODIS observations. The annual amplitude range from ~1 cm in the northwest to ~10 cm in the southeast and the semiannual amplitude range from ~1 cm to ~5 cm. The spatial patterns correlate with the topography (Figure 4c). The amplitudes vary smoothly in space except where there is significant topographic relief. The maximum spatial variations of annual and semiannual amplitudes of ~9 and ~4 cm correspond to maximum relative LOS displacement biases of ~23.8 and 10.6 cm, respectively, between epochs for an incidence angle of 41°.

To obtain the displacement uncertainties due to the stochastic component of the delay, we first estimate for all MODIS pixels the standard deviation of the absolute residual slant wet delay time series (Figure 5a), which we obtain using equation (6) by subtracting the seasonal delay from the wet delay and projecting the result into LOS direction. Next, we calculate the covariance of the time series of residual slant wet delay relative to the reference pixels of the seven SAR tracks (Figure 5b). Finally, we use equation (7) to obtain the displacement uncertainties relative to the reference pixels (Figure 5c). These relative uncertainties represent the scatter of the relative InSAR time series due to the temporally stochastic component of the tropospheric delay. The map of absolute standard deviation (Figure 5a) shows that $\sigma_{\text{RSWD}(\rho)}$ varies from ~2 cm in the northwest in the Rigestan desert to ~8 to ~9 cm in the southern and eastern parts. The map of relative uncertainties

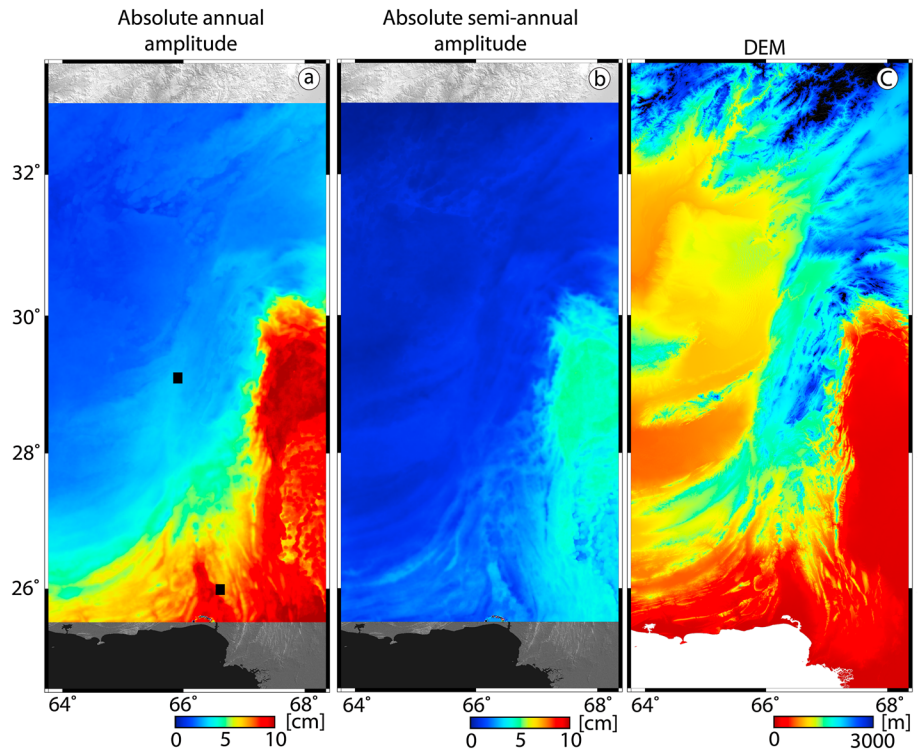


Figure 4. Amplitude of (a) annual and (b) semiannual absolute ZWD from MODIS observations. (c) Digital elevation model from Shuttle Radar Topography Mission for the study area. The black squares in Figure 4a indicate the location of the two pixels of which their delay time series were evaluated in Figures 2 and 3.

(Figure 5c) shows that $\sigma_{\text{RSWD}(p) - \text{RSWD}(\text{ref})}$ increases with distance from the reference pixels and reaches up to ~ 6 cm in the southern parts of the tracks 27, 256, and 485. The spatial variation of $\sigma_{\text{RSWD}(p) - \text{RSWD}(\text{ref})}$ is discussed in more detail in section 5.2.

4.2.2. After Tropospheric Delay Correction

To evaluate the uncertainty of InSAR displacement time series corrected for the stratified tropospheric delay, we obtain a second residual slant wet delay by subtracting the wet delay of the ERA-I model from the MODIS wet delay and projecting into slant direction (using equation (9)). For this residual slant wet delay we also estimate the covariance with respect to the reference pixels and then obtain the uncertainty (using equation (7)). The obtained uncertainty map (Figure 5d) represents the scatter of the InSAR time series due to the residual wet delay after stratified tropospheric delay correction. The uncertainty increases from the reference pixels to up to ~ 5 cm. The uncertainties after stratified tropospheric delay correction (Figure 5d) are smaller than for the stochastic delays without correction (Figure 5c), which is discussed in detail in section 5.2.

4.3. Uncertainty of InSAR Velocity Due To the Stochastic Delay

4.3.1. Without Stochastic Tropospheric Delay Correction (Seasonal Delay Is Removed)

Figure 6a shows the velocity uncertainties for the Envisat tracks obtained from the residual of MODIS and the best fitting seasonal delay relative to the reference pixels. The uncertainties were obtained from Figure 5c and using the SAR acquisition times (using equation (8)). The map shows that for each track the relative uncertainties are zero near the reference point and increase with distance to up to 4–5 mm/yr for tracks 299 and 256. The highest relative uncertainties of ~ 8 mm/yr occur in southern parts of tracks 485 and 213.

4.3.2. After Stratified Tropospheric Delay Correction

4.3.2.1. Uncertainty From Residual of MODIS and ERA-I Wet Delay

Figure 6b shows the same as Figure 6a but for the residual of MODIS and ERA-I. The map was obtained from Figure 5d and the SAR acquisition times (using equation (8)). The uncertainty map is very similar to Figure 6a, but the uncertainties are generally smaller, which is discussed in section 5.2.

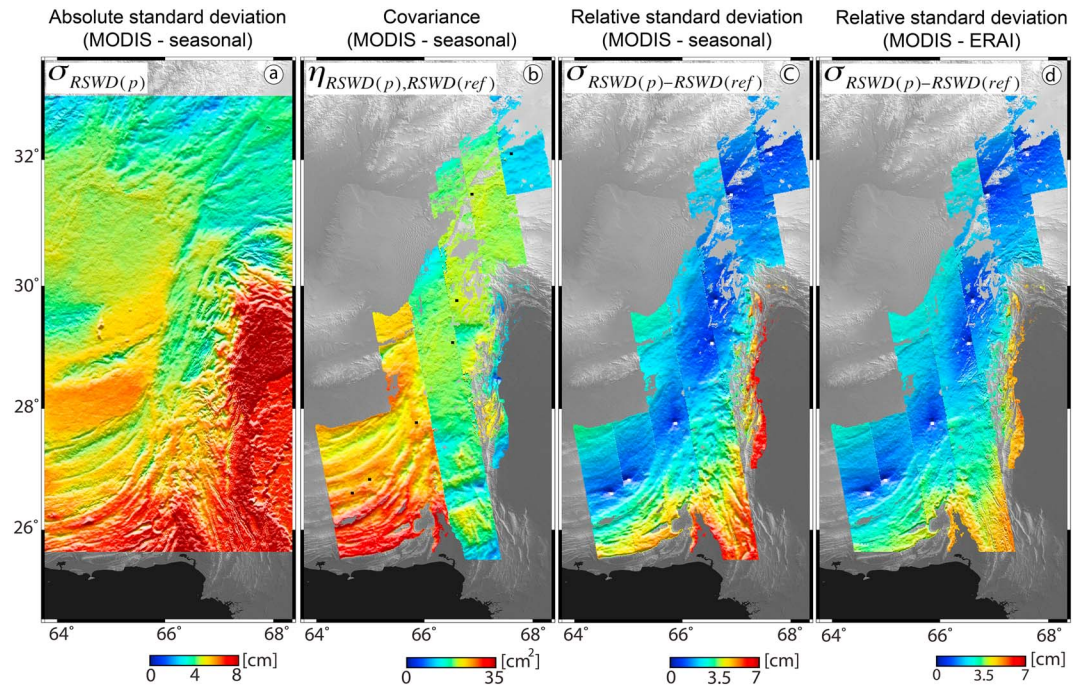


Figure 5. (a) Standard deviation of residual slant wet delay (RSWD) from MODIS (seasonal bias removed); (b) covariance of residual slant wet delay between all pixels and the reference pixels of each track; (c) standard deviation of residual relative delay from MODIS (seasonal bias removed), representing the uncertainty due to stochastic delay for displacement time series; and (d) same after subtraction of stratified wet delay using ERA-I. Figure 5c is the same as Figure 5a but relative to the reference pixels. Smaller uncertainties in Figure 5d compared to Figure 5c show that the stratified tropospheric delay correction with ERA-I reduces the variance of the stochastic component of wet delay. Figure 5a shows absolute values at each pixel, and Figures 5b–5d show relative values at each pixel with respect to the reference pixels at each track.

4.3.2.2. Uncertainty From InSAR Range Change Time Series After Stratified Delay Correction Using ERA-I

We also obtain uncertainties from the scatter of the InSAR range change time series (using equation (10), Figure 6c). The range change time series are corrected for wet and hydrostatic stratified delay using the ERA-I model, for topographic residuals, and for local oscillator drift but not for inaccuracies of the satellite orbits. Hence, the uncertainties represent the stochastic component of the tropospheric delay as well as orbital errors.

5. Discussion

We divided the temporal variation of the tropospheric wet delay into systematic and stochastic components. We modeled the systematic component as seasonal delay with annual and semiannual periodicities and analyzed the stochastic component, obtained by subtracting the systematic component from the wet delay. We evaluated both the bias due to the systematic component and the uncertainty due to the stochastic component on relative InSAR measurements.

5.1. Displacement and Velocity Bias Due To the Seasonal Delay

The time series of wet delay from MODIS and ERA-I for the western India plate boundary show a systematic, temporally correlated component dominated by seasonal variations with annual and semiannual periodicities. The seasonal variations skew the distribution of the delay and bias the InSAR displacement time series and velocities.

The magnitudes of the biases are a linear function of the amplitudes of the seasonal delay and a nonlinear function of the SAR acquisition times. The absolute amplitudes vary smoothly in space. Therefore, the impact of the seasonal delay on relative displacement measurements is smaller between pixels at short distances and similar elevations than between pixels at large distances and different elevations. The displacement bias is largest between the peak and trough of a seasonal cycle and vanishes for acquisitions one year apart.

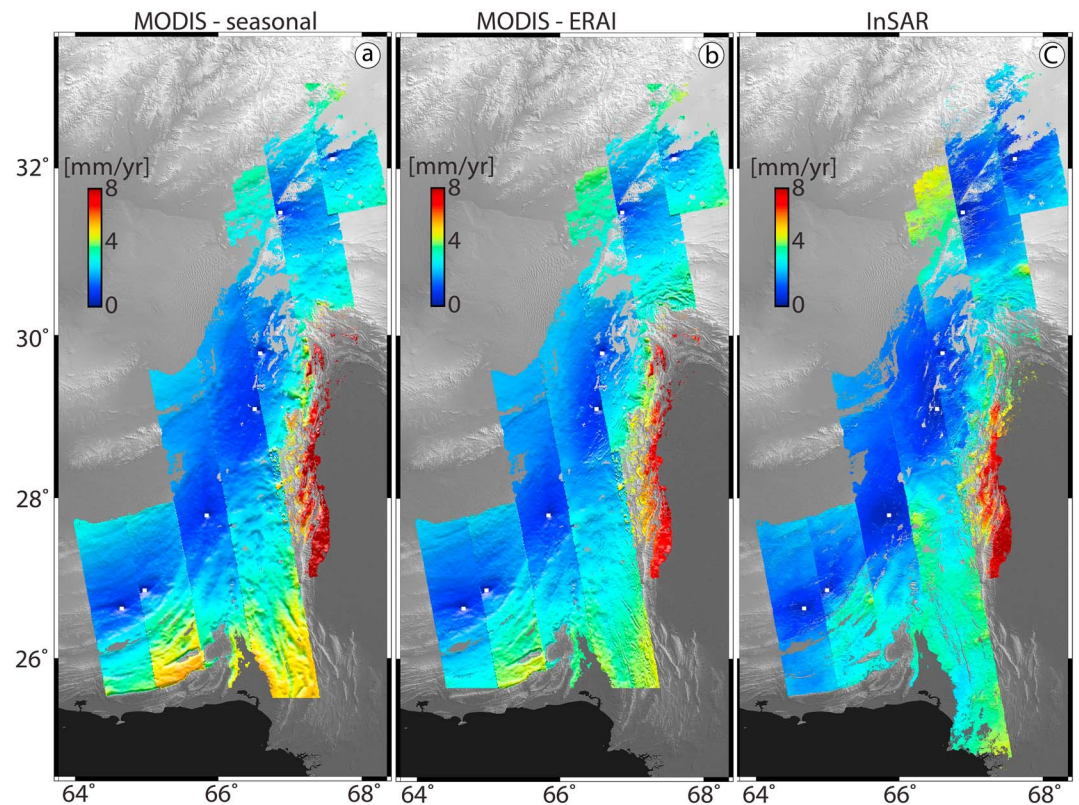


Figure 6. Uncertainty of the InSAR velocity fields relative to the reference pixels (white boxes) obtained from (a) the residual of MODIS and seasonal delay, (b) the residual of MODIS and ERA-I, and (c) InSAR range change time series (σ_v^{InSAR}). Figures 6a and 6b were obtained from Figures 5c and 5d, respectively, using equation (8) and given the SAR acquisition times.

In contrast to the velocity uncertainty, using more acquisitions does not necessarily reduce the bias on velocity. Low-pass temporal or spatial-temporal filtering approaches [e.g., *Ferretti et al., 2001; Bernardino et al., 2002*] can produce biased displacement time series and velocities, because the assumption implicit in these approaches that the scatter of the atmospheric delay is temporally uncorrelated Gaussian noise is violated by the seasonal delay.

The stratified tropospheric delay correction mitigates the effects of the systematic, seasonal delay [*Doin et al., 2009; Jolivet et al., 2011; Jolivet et al., 2014*], largely eliminating the biases, as shown by the good agreement between the uncertainties obtained from the stochastic component of the wet delay (Figure 5c) and after subtracting the ERA-I wet delay from the MODIS wet delay (Figure 5d).

5.2. Uncertainties Due To Stochastic Delay and Implicit Assumptions

We have obtained uncertainties for relative InSAR displacement time series using two different approaches. In the first approach we have assumed that the systematic component of the wet delay is seasonal and that it can be modeled by annual and semiannual periodicities. After removal of seasonal delay and projection of the residual into slant direction (equation (6)), the scatter of the residual delay represents the uncertainty of InSAR displacement time series due to stochastic tropospheric delay variations. In the second approach we obtained uncertainties from the residual after stratified delay correction (equation (9)). In both approaches, we obtained uncertainties for velocity using linear error propagation (equation (8)).

Uncertainties of displacement time series and velocities are smaller after stratified delay correction compared to the uncertainties obtained using the seasonal model (Figure 5d versus Figure 5c and Figure 6b versus Figure 6a). Possible explanations for the smaller uncertainties after the stratified delay correction are (i) that the ERA-I model does a better job removing the systematic component of the delay than the periodic model of equation (3) and (ii) that the stratified delay calculated from ERA-I contains not only seasonal variations but also a portion of the temporally random component.

The implicit assumption in both approaches is that the scatter of the residual wet delay has the character of temporally uncorrelated Gaussian noise. This assumption could be violated by the leakage of temporally correlated delay into the residual, because it is not captured by the periodic model and/or by the atmospheric model.

5.3. Effect of the Covariance of Noise

The uncertainty for the LOS displacement measurement between two given pixels depends also on the covariance of the stochastic tropospheric delay (equation (7)). The covariance between the two pixels is related to their standard deviations at each pixel and the correlation between the two pixels as $\eta_{\text{RSWD}(p), \text{RSWD}(q)} = \rho \sigma_{\text{RSWD}(p)} \sigma_{\text{RSWD}(q)}$, where ρ is the correlation between $\text{RSWD}(p)$ and $\text{RSWD}(q)$. If the tropospheric delay between the two pixels is fully correlated ($\rho = 1$) and the variances of the residual slant wet delay for the two pixels are the same $\sigma_{\text{RSWD}(p)} \approx \sigma_{\text{RSWD}(q)}$, then substituting into equation (7) gives $\sigma_{\text{RSWD}(p) - \text{RSWD}(q)} \approx 0$, which means that the uncertainty due to the tropospheric delay between the two pixels is negligible.

As the troposphere variation is small over short distances, the temporally stochastic delay is highly correlated for closely spaced pixels, leading to small uncertainties based on equation (7). As the troposphere variation increases with distance, the correlation of the stochastic delay decreases, leading to larger uncertainties between pixels farther apart. The increase of the uncertainties with distance from the reference pixel is evident in Figures 5c, 5d, and 6. Note that such increase with distance is not expected for the map of covariance (Figure 5b), because covariance of stochastic delay between each pixel and itself represents the variance of the absolute stochastic delay at that pixel.

5.4. InSAR Uncertainty Dominated by Stochastic Delay

We compared the uncertainties obtained from the residual of MODIS and ERA-I (Figure 6b) with the uncertainties derived from the scatter of the InSAR range change time series. These two uncertainties are very similar in pattern and magnitude. The correlation coefficient between the two uncertainties is 0.88 (see supporting information Figure S3). From this we infer that the sources for uncertainty are nearly identical in both cases, implying that the scatter of the range change InSAR time series after the stratified tropospheric delay correction is largely due to residual tropospheric delay. It also implies that the corrections applied to the range change data (stratified tropospheric delay correction and topographic residual) have eliminated most of the biases.

The residual tropospheric delay is due to the inaccuracy of the global atmospheric model and nonstratified (turbulent) delay. Both components could likely be reduced using higher spatial and higher temporal resolution weather models, which would lead to more accurate and precise measurements.

The uncertainties obtained from the range change time series include a component introduced by the uncertainties of the satellite orbits. Given Envisat's precise orbits, this uncertainty is less than 0.5 mm/yr/100 km in both range and azimuth directions [Fattahi and Amelung, 2014]. The similarities of the uncertainties from the range change time series and MODIS suggest that the contribution from orbital errors is small (in particular in azimuth direction), consistent with Fattahi and Amelung [2014].

5.5. InSAR Variance-Covariance Matrix

The interpretation of InSAR-measured ground velocities in terms of the geophysical processes causing the observed ground deformation requires information on the uncertainty of the velocity between any pair of coherent pixels, expressed by a variance-covariance matrix, C_n , which is the sum of three independent components as

$$C_n = C_{\text{decor}} + C_{\text{orbit}} + C_{\text{trop}} \quad (11)$$

where C_{decor} represents the variance-covariance matrix from phase decorrelation, C_{orbit} from orbital errors, and C_{trop} from stochastic tropospheric delay. Here we have neglected components from ionospheric delay and from phase-unwrapping errors. C_{decor} is given by Agram and Simons [2015] for displacement time series, which can be propagated for the velocity, and C_{orbit} is given by Fattahi and Amelung [2014] for velocity. A full variance-covariance matrix of displacement for M pixels at a time series epoch relative to a reference epoch can be expressed as [Agram and Simons, 2015, equation (9)]

$$C_{\text{trop}} = \begin{bmatrix} \eta_{1,1} & \cdots & \eta_{1,M} \\ \vdots & & \vdots \\ \eta_{M,1} & \cdots & \eta_{M,M} \end{bmatrix} \quad (12)$$

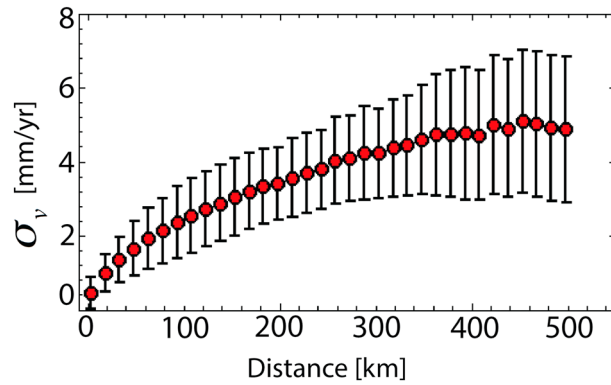


Figure 7. Average and standard deviation of the relative LOS velocity uncertainty, σ_v^{insar} , as a function of relative distance between pixels, obtained from random samples of 500 pixels for each track.

where $\eta_{p,q}$ is the covariance of the stochastic delay between pixels p and q . The diagonal elements are the variances of the absolute stochastic delay (Figure 5a), and the nondiagonal elements are the covariances between all possible pairs of pixels, which are related to the absolute and relative variances as

$$\eta_{p,q} = \frac{1}{2} \left(\sigma_{\text{RSWD}(p)}^2 + \sigma_{\text{RSWD}(q)}^2 - \sigma_{\text{RSWD}(p)-\text{RSWD}(q)}^2 \right) \quad (13)$$

Given the full covariance matrices for all time series epochs, the uncertainty can be propagated to the velocity (see supporting

information). However, note that the map of covariances in Figure 5b for each track is relative to the reference pixels. Given M pixels, $\frac{M \times (M-1)}{2}$ similar map of covariances are required considering all possible reference pixels to form the full variance-covariance matrix of the displacement, which is computationally expensive [Agram and Simons, 2015]. For example, a region with 1000×1000 pixels requires $\sim 5 \times 10^{11}$ covariance maps similar to Figure 5b. Therefore, in the following we develop an efficient approach to estimate C_{trop} for velocity using the relative uncertainties from the previous sections.

As the calculation is computationally expensive for the entire region, we select for each track a random sample of 500 coherent pixels and estimate the relative velocity uncertainty between all possible pairs of pixels within this sample (see Figures S4a–S4h for plots of the uncertainties versus distance for each and all tracks). The averages and standard deviations of the uncertainties binned over 15 km distance intervals both increase with distance (Figure 7) until they flatten out at a distance of ~ 360 km beyond which the noise is uncorrelated.

Assuming isotropic noise, which implies that the covariance of noise between a pair of pixels only depends on their distance but not on their location and/or relative orientation [Lohman and Simons, 2005], we can populate the full covariance matrix of the InSAR velocity field as a function of the distance between the two pixels as

$$C_{ij} = \begin{cases} \sigma_s^2 - \sigma^2(r), & i \neq j \\ \sigma_s^2, & i = j \end{cases}, \forall i, j \in [1, P] \quad (14)$$

where C_{ij} is the covariance of noise between pixels i and j , $\sigma(r)$ is the velocity uncertainty for distance r between the pixels, σ_s is a sill value (5 mm/yr at 360 km distance), and P is the number of pixels.

The covariogram of Figure 7 is similar to the structure functions, which are commonly used to form the variance-covariance matrix of InSAR data [Lohman and Simons, 2005; Sudhaus and Jónsson, 2009; Jolivet et al., 2012; Bekaert et al., 2015b; González and Fernández, 2011]. The structure functions are usually obtained from a specific region of the study area and are based on the assumption that the region is not affected by ground deformation. In contrast, our approach for estimating the velocity uncertainty is based on a sample of pixels from the whole area and is independent of linear ground deformation. It is computationally efficient because the 500 pixels for each track require the calculation for 124,750 pairs, compared to 10^{12} possible pairs for all the 4×10^6 pixels of track 256. Given the relative uncertainties for displacement (Figure 5d), the same approach can be used to form the variance-covariance matrix of displacement between any two epochs.

6. Conclusion

We have analyzed the systematic and stochastic components of the tropospheric wet delay affecting the InSAR range change measurement and presented an approach to estimate the uncertainty of InSAR displacement time series and velocity fields due to the tropospheric delay. This approach is based on MODIS precipitable water vapor observations and atmospheric models. The findings of this study are as follows:

1. The systematic component of the tropospheric delay arises because of seasonal variations in the moisture content of the atmosphere. It biases the InSAR displacements and velocities. The magnitude of the bias depends on the amplitude of the seasonal variations (we assume annual and semiannual periodicities) and the sampling of the seasonal cycle by SAR acquisitions. The displacement bias is largest between two epochs at the peak and trough of a cycle and vanishes between epochs one year apart. A larger number of SAR acquisitions does not necessarily reduce the velocity bias.
2. The velocity uncertainty due to the stochastic component of the tropospheric delay between two pixels depends on the standard deviation of the distribution of the random delay and is inversely proportional to the number of SAR acquisitions and the total time span covered. The uncertainty also depends on the covariance of the random tropospheric delay between the two pixels. It is smaller between pixels at short distances than between pixels at long distances.
3. Along the western India plate boundary, the amplitudes of the annual and semiannual components vary up to ~ 10 and ~ 5 cm, respectively. The relative variation between two pixels is up to 9 and 4 cm, respectively, corresponding to up to 18 and 8 cm between two epochs and to a bias of up to 23.8 and 10.6 cm in LOS direction assuming a radar incidence angle of 41° for the Envisat ASAR IS6 mode.
4. The residual of the time series of wet delay from MODIS and ERA-I can be used to quantify the uncertainty of the InSAR displacement time series and velocity fields corrected for stratified tropospheric delay. Along the western India plate boundary, this velocity uncertainty is consistent with the velocity uncertainty obtained from the scatter of the InSAR range change time series (corrected for the local oscillator drift, topographic residuals, and stratified tropospheric delay). This shows that the scatter of the InSAR range change time series is dominated by the residual tropospheric delay and not affected by any significant systematic noise.

Acknowledgments

The MODIS PWV data of NASA's Aqua and Terra satellites were obtained using the Jet Propulsion Laboratory's Online Services for Correcting Atmosphere in Radar (OSCAR). The SAR raw data from ESA's Envisat satellite were obtained using UNAVCO's Seamless SAR archive (SSARA). We thank Brian Mapes from the UM Atmospheric Sciences Department and Shimon Wdowinski for discussions. This study was funded by grants from NASA's Earth Science division and the National Science Foundation's tectonics program to F.A. (NNX09AD22G and EAR-1019847).

References

- Agram, P. S., and M. Simons (2015), A noise model for InSAR time series, *J. Geophys. Res. Solid Earth*, *120*, 2752–2771, doi:10.1002/2014JB011271.
- Amelung, F., D. L. Galloway, J. W. Bell, H. A. Zebker, and R. J. Lacznik (1999), Sensing the ups and downs of Las Vegas: InSAR reveals structural control of land subsidence and aquifer-system deformation, *Geology*, *27*(6), 483–486.
- Bekaert, D. P. S., A. Hooper, and T. J. Wright (2015a), A spatially-variable power-law tropospheric correction technique for InSAR data, *J. Geophys. Res. Solid Earth*, *120*, 1345–1356, doi:10.1002/2014JB011558.
- Bekaert, D. P. S., A. Hooper, and T. J. Wright (2015b), Reassessing the 2006 Guerrero slow-slip event, Mexico: Implications for large earthquakes in the Guerrero Gap, *J. Geophys. Res. Solid Earth*, *120*, 1357–1375, doi:10.1002/2014JB011557.1.
- Berardino, P., G. Fornaro, R. Lanari, S. Member, and E. Sansosti (2002), A new algorithm for surface deformation monitoring based on small baseline differential SAR interferograms, *IEEE Trans. Geosci. Remote Sens.*, *40*(11), 2375–2383.
- Bevis, M., S. Businger, S. Chiswell, T. A. Herring, R. A. Anthes, C. Rocken, and R. H. Ware (1994), GPS meteorology: Mapping zenith wet delays onto precipitable water, *J. Appl. Meteorol.*, *33*(3), 379–386.
- Biggs, J., T. Wright, Z. Lu, and B. Parsons (2007), Multi-interferogram method for measuring interseismic deformation: Denali Fault, Alaska, *Geophys. J. Int.*, *170*(3), 1165–1179.
- Calais, E., A. Freed, G. Mattioli, F. Amelung, S. Jónsson, P. Jansma, S.-H. Hong, T. Dixon, C. Prépetit, and R. Mompalao (2010), Transpressional rupture of an unmapped fault during the 2010 Haiti earthquake, *Nat. Geosci.*, *3*(11), 794–799.
- Chaussard, E., F. Amelung, and Y. Aoki (2013), Characterization of open and closed volcanic systems in Indonesia and Mexico using InSAR time series, *J. Geophys. Res. Solid Earth*, *118*, 3957–3969, doi:10.1002/jgrb.50288.
- Chen, A. C., S. Member, and H. A. Zebker (2014), Reducing ionospheric effects in InSAR data using accurate coregistration, *IEEE Geosci. Remote Sens. Soc.*, *52*(1), 60–70.
- Chen, J., S. Member, and H. A. Zebker (2012), Ionospheric artifacts in simultaneous L-band InSAR and GPS observations, *IEEE Geosci. Remote Sens. Soc.*, *50*(4), 1227–1239.
- Cong, X., U. Balss, M. Eineder, and T. Fritz (2012), Imaging geodesy—Centimeter-level ranging accuracy with TerraSAR-X: An update, *IEEE Geosci. Remote Sens. Soc.*, *9*(5), 948–952.
- Dee, D. P., et al. (2011), The ERA-Interim reanalysis: Configuration and performance of the data assimilation system, *Q. J. R. Meteorol. Soc.*, *137*(656), 553–597, doi:10.1002/qj.828.
- Dehghani, M., M. J. V. Zojj, I. Entezam, A. Mansourian, and S. Saatchi (2009), InSAR monitoring of progressive land subsidence in Neyshabour, northeast Iran, *Geophys. J. Int.*, *178*(1), 47–56.
- Doin, M.-P., C. Lasserre, G. Peltzer, O. Cavalié, and C. Doubre (2009), Corrections of stratified tropospheric delays in SAR interferometry: Validation with global atmospheric models, *J. Appl. Geophys.*, *69*(1), 35–50, doi:10.1016/j.jappgeo.2009.03.010.
- Eff-Darwich, A., J. C. Pérez, J. Fernández, B. García-Lorenzo, A. González, and P. J. González (2012), Using a mesoscale meteorological model to reduce the effect of tropospheric water vapour from DInSAR data: A case study for the island of Tenerife, Canary Islands, *Pure Appl. Geophys.*, *169*(8), 1425–1441.
- Emardson, T. R. (2003), Neutral atmospheric delay in interferometric synthetic aperture radar applications: Statistical description and mitigation, *J. Geophys. Res.*, *108*(B5), 2231, doi:10.1029/2002JB001781.
- Fattahi, H. (2015), *Geodetic Imaging of Tectonic Deformation With InSAR*, Doctoral dissertation, Univ. of Miami.
- Fattahi, H., and F. Amelung (2013), DEM error correction in InSAR time series, *IEEE Trans. Geosci. Remote Sens.*, *51*(7), 4249–4259, doi:10.1109/tgrs.2012.2227761.
- Fattahi, H., and F. Amelung (2014), InSAR uncertainty due to orbital errors, *Geophys. J. Int.*, *199*(1), 549–560, doi:10.1093/gji/ggu276.

- Ferretti, A., C. Prati, and F. Rocca (2001), Permanent scatterers in SAR interferometry, *IEEE Trans. Geosci. Remote Sens.*, *39*(1), 8–20.
- Foster, J., B. Brooks, T. Cherubini, C. Shacat, S. Businger, and C. L. Werner (2006), Mitigating atmospheric noise for InSAR using a high resolution weather model, *Geophys. Res. Lett.*, *33*, L16304, doi:10.1029/2006GL026781.
- Foster, J., J. Kealy, T. Cherubini, S. Businger, Z. Lu, and M. Murphy (2013), The utility of atmospheric analyses for the mitigation of artifacts in InSAR, *J. Geophys. Res. Solid Earth*, *118*, 748–758, doi:10.1002/jgrb.50093.
- Fournier, T., M. E. Pritchard, and N. Finnegan (2011), Accounting for atmospheric delays in InSAR data in a search for long-wavelength deformation in South America, *IEEE Trans. Geosci. Remote Sens.*, *49*(10), 3856–3867.
- Funning, G. J., B. Parsons, T. J. Wright, J. A. Jackson, and E. J. Fielding (2005), Surface displacements and source parameters of the 2003 Bam (Iran) earthquake from Envisat advanced synthetic aperture radar imagery, *J. Geophys. Res.*, *110*, B09406, doi:10.1029/2004JB003338.
- Goldstein, R. (1995), Atmospheric limitations to repeat-track radar interferometry, *Geophys. Res. Lett.*, *22*(18), 2517–2520.
- Gong, W., F. J. Meyer, S. Liu, and R. F. Hanssen (2015), Temporal filtering of InSAR data using statistical parameters from NWP models, *IEEE Trans. Geosci. Remote Sens.*, *53*, 1–12.
- González, P. J., and J. Fernández (2011), Error estimation in multitemporal InSAR deformation time series, with application to Lanzarote, Canary Islands, *J. Geophys. Res.*, *116*, B10404, doi:10.1029/2011JB008412.
- Grandin, R., M.-P. Doin, L. Bollinger, B. Pinel-Puysségur, G. Ducret, R. Jolivet, and S. N. Sapkota (2012), Long-term growth of the Himalaya inferred from interseismic InSAR measurement, *Geology*, *40*(12), 1059–1062.
- Hanssen, R. F. (2001), *Radar Interferometry: Data Interpretation and Error Analysis*, Springer Science & Business Media, Netherlands.
- Hobiger, T., Y. Kinoshita, S. Shimizu, R. Ichikawa, M. Furuya, T. Kondo, and Y. Koyama (2010), On the importance of accurately ray-traced troposphere corrections for Interferometric SAR data, *J. Geod.*, *84*(9), 537–546, doi:10.1007/s00190-010-0393-3.
- Jolivet, R., R. Grandin, C. Lasserre, M.-P. Doin, and G. Peltzer (2011), Systematic InSAR tropospheric phase delay corrections from global meteorological reanalysis data, *Geophys. Res. Lett.*, *38*, L17311, doi:10.1029/2011GL048757.
- Jolivet, R., C. Lasserre, M.-P. Doin, S. Guillaso, G. Peltzer, R. Dailu, J. Sun, Z.-K. Shen, and X. Xu (2012), Shallow creep on the Haiyuan Fault (Gansu, China) revealed by SAR Interferometry, *J. Geophys. Res.*, *117*, B06401, doi:10.1029/2011JB008732.
- Jolivet, R., P. S. Agram, N. Y. Lin, M. Simons, M. Doin, G. Peltzer, and Z. Li (2014), Improving InSAR geodesy using Global Atmospheric Models, *J. Geophys. Res. Solid Earth*, *119*, 2324–2341, doi:10.1002/2013JB010588.
- Kinoshita, Y., M. Furuya, T. Hobiger, and R. Ichikawa (2013), Are numerical weather model outputs helpful to reduce tropospheric delay signals in InSAR data?, *J. Geod.*, *87*(3), 267–277.
- Li, Z., J. P. Muller, and P. Cross (2003), Comparison of precipitable water vapor derived from radiosonde, GPS, and Moderate-Resolution Imaging Spectroradiometer measurements, *J. Geophys. Res.*, *108*(D20), 4651, doi:10.1029/2003JD003372.
- Li, Z., J.-P. Muller, P. Cross, and E. J. Fielding (2005), Interferometric synthetic aperture radar (InSAR) atmospheric correction: GPS, Moderate Resolution Imaging Spectroradiometer (MODIS), and InSAR integration, *J. Geophys. Res.*, *110*, B03410, doi:10.1029/2004JB003446.
- Li, Z., E. J. Fielding, P. Cross, and J.-P. Muller (2006), Interferometric synthetic aperture radar atmospheric correction: Medium Resolution Imaging Spectrometer and Advanced Synthetic Aperture Radar integration, *Geophys. Res. Lett.*, *33*, L06816, doi:10.1029/2005GL025299.
- Li, Z., E. J. Fielding, P. Cross, and R. Preusker (2009), Advanced InSAR atmospheric correction: MERIS/MODIS combination and stacked water vapour models, *Int. J. Remote Sens.*, *30*(13), 3343–3363, doi:10.1080/01431160802562172.
- Lin, Y. N., M. Simons, E. A. Hetland, P. Muse, and C. DiCaprio (2010), A multiscale approach to estimating topographically correlated propagation delays in radar interferograms, *Geochem. Geophys. Geosyst.*, *11*, Q09002, doi:10.1029/2010GC003228.
- Liu, S. (2012), Satellite radar interferometry: Estimation of atmospheric delay PhD dissertation, Geosci. Remote Sens., Delft Univ. Technol., Delft, Netherlands.
- Liu, Z., H.-S. Jung, and Z. Lu (2014), Joint correction of ionosphere noise and orbital error in L-band SAR interferometry of interseismic deformation in Southern California, *IEEE Trans. Geosci. Remote Sens.*, *52*(6), 3421–3427.
- Löfgren, J. S., F. Björndahl, A. W. Moore, F. H. Webb, E. J. Fielding, and E. F. Fishbein (2010), Tropospheric correction for InSAR using interpolated ECMWF data and GPS zenith total delay from the Southern California integrated GPS network, in *Geoscience and Remote Sensing Symposium (IGARSS), 2010 IEEE International*, pp. 4503–4506, IEEE, Honolulu, Hawaii.
- Lohman, R. B., and M. Simons (2005), Some thoughts on the use of InSAR data to constrain models of surface deformation: Noise structure and data downsampling, *Geochem. Geophys. Geosyst.*, *6*, Q01007, doi:10.1029/2004GC000841.
- Lu, N., J. Qin, K. Yang, Y. Gao, X. Xu, and T. Koike (2011), On the use of GPS measurements for Moderate Resolution Imaging Spectrometer precipitable water vapor evaluation over southern Tibet, *J. Geophys. Res.*, *116*, D23117, doi:10.1029/2011JD016160.
- Marinkovic, P., and Y. Larsen (2013), Consequences of long-term ASAR local oscillator frequency decay—An empirical study of 10 years of data, in *Living Planet Symposium*, Edinburgh, U. K.
- Massonnet, D., and K. L. Feigl (1995), Satellite radar interferometric map of the coseismic deformation field of the $M = 6.1$ Eureka Valley, California earthquake of May 17, 1993, *Geophys. Res. Lett.*, *22*(12), 1541–1544.
- Massonnet, D., and K. L. Feigl (1998), Radar interferometry and its application to changes in the Earth's surface, *Rev. Geophys.*, *36*(4), 441–500.
- Mattar, K. E., and A. L. Gray (2002), Reducing ionospheric electron density errors in satellite radar interferometry applications, *Can. J. Remote Sens.*, *28*(4), 593–600.
- Mendes, V. (1999), *Modeling the Neutral-Atmospheric Propagation Delay in Radiometric Space Techniques*, UNB, Brunswick.
- Onn, F., and H. A. Zebker (2006), Correction for interferometric synthetic aperture radar atmospheric phase artifacts using time series of zenith wet delay observations from a GPS network, *J. Geophys. Res.*, *111*, B09102, doi:10.1029/2005JB004012.
- Pepe, A., R. Lanari, and S. Member (2006), On the extension of the minimum cost flow algorithm for phase unwrapping of multitemporal differential SAR interferograms, *IEEE Trans. Geosci. Remote Sens.*, *44*(9), 2374–2383.
- Prasad, A. K., and R. P. Singh (2009), Validation of MODIS Terra, AIRS, NCEP/DOE AMIP-II Reanalysis-2, and AERONET Sun photometer derived integrated precipitable water vapor using ground-based GPS receivers over India, *J. Geophys. Res.*, *114*, D05107, doi:10.1029/2008JD011230.
- Pritchard, M. E., J. A. Jay, F. Aron, S. T. Henderson, and L. E. Lara (2013), Subsidence at southern Andes volcanoes induced by the 2010 Maule, Chile earthquake, *Nat. Geosci.*, *6*(8), 632–636.
- Puysségur, B., R. Michel, and J.-P. Avouac (2007), Tropospheric phase delay in interferometric synthetic aperture radar estimated from meteorological model and multispectral imagery, *J. Geophys. Res.*, *112*, B05419, doi:10.1029/2006JB004352.
- Rosen, P. A., S. Hensley, I. R. Joughin, F. K. Li, S. N. Madsen, E. Rodriguez, and R. M. Goldstein (2000), Synthetic aperture radar interferometry, *Proc. IEEE*, *88*(3), 333–382.
- Rosen, P., S. Hensley, and C. Chen (2010), Measurement and mitigation of the ionosphere in L-band interferometric SAR data, in *Radar Conference, 2010 IEEE*, pp. 1459–1463, IEEE, Washington, D. C.
- Samsonov, S. (2010), Topographic correction for ALOS PALSAR interferometry, *IEEE Trans. Geosci. Remote Sens.*, *48*(7), 3020–3027.

- Samsonov, S. V., A. P. Trishchenko, K. Tiampo, P. J. González, Y. Zhang, and J. Fernández (2014), Removal of systematic seasonal atmospheric signal from interferometric synthetic aperture radar ground deformation time series, *Geophys. Res. Lett.*, *41*, 6123–6130, doi:10.1002/2014GL061307.
- Schmidt, D. A., R. Bürgmann, R. M. Nadeau, and M. d'Alessio (2005), Distribution of aseismic slip rate on the Hayward fault inferred from seismic and geodetic data, *J. Geophys. Res.*, *110*, B08406, doi:10.1029/2004JB003397.
- Simons, M., Y. Fialko, and L. Rivera (2002), Coseismic deformation from the 1999 Mw 7.1 Hector Mine, California, earthquake as inferred from InSAR and GPS observations, *Bull. Seismol. Soc. Am.*, *92*(4), 1390–1402.
- Smith, E. K., and S. Weintraub (1953), The constants in the equation for atmospheric refractive index at radio frequencies, *Proc. IRE*, *41*(8), 1035–1037.
- Sudhaus, H., and S. Jónsson (2009), Improved source modelling through combined use of InSAR and GPS under consideration of correlated data errors: Application to the June 2000 Kleifarvatn earthquake, Iceland, *Geophys. J. Int.*, *176*(2), 389–404, doi:10.1111/j.1365-246X.2008.03989.x.
- Tarayre, H., and D. Massonnet (1996), Atmospheric propagation heterogeneities revealed by ERS-1 interferometry, *Geophys. Res. Lett.*, *23*(9), 989–992.
- Thomas, I. D., M. A. King, P. J. Clarke, and N. T. Penna (2011), Precipitable water vapor estimates from homogeneously reprocessed GPS data: An intertechnique comparison in Antarctica, *J. Geophys. Res.*, *116*, D04107, doi:10.1029/2010JD013889.
- Wadge, G., M. Zhu, R. J. Holley, I. N. James, P. A. Clark, C. Wang, and M. J. Woodage (2010), Correction of atmospheric delay effects in radar interferometry using a nested mesoscale atmospheric model, *J. Appl. Geophys.*, *72*(2), 141–149.
- Walters, R. J., J. R. Elliott, Z. Li, and B. Parsons (2013), Rapid strain accumulation on the Ashkabad fault (Turkmenistan) from atmosphere-corrected InSAR, *J. Geophys. Res. Solid Earth*, *118*, 3674–3690, doi:10.1002/jgrb.50236.
- Wang, L., R. Wang, F. Roth, B. Enescu, S. Hainzl, and S. Ergintav (2009), Afterslip and viscoelastic relaxation following the 1999 M 7.4 İzmit earthquake from GPS measurements, *Geophys. J. Int.*, *178*(3), 1220–1237, doi:10.1111/j.1365-246X.2009.04228.x.
- Wang, T., and S. Jonsson (2014), Phase-ramp reduction in interseismic interferograms from pixel-offsets, *IEEE J. Sel. Top. Appl. Earth Obs. Remote Sens.*, *5*(7), 1709–1718.
- Webley, P. W., G. Wadge, and I. N. James (2004), Determining radio wave delay by non-hydrostatic atmospheric modelling of water vapour over mountains, *Phys. Chem. Earth, Parts A/B/C*, *29*(2), 139–148.
- Wei, M., D. Sandwell, and B. Smith-Konter (2010), Optimal combination of InSAR and GPS for measuring interseismic crustal deformation, *Adv. Space Res.*, *46*(2), 236–249.
- Zebker, H. A., P. A. Rosen, and S. Hensley (1997), Atmospheric effects in interferometric synthetic aperture radar surface deformation and topographic maps, *J. Geophys. Res.*, *102*(B4), 7547–7563.
- Zebker, H., and J. Villasenor (1992), Decorrelation in interferometric radar echoes, *IEEE Trans. Geosci. Remote Sens.*, *30*(5), 950–959.